SAE INTERNATIONAL

ARTICLE INFO
Article ID: 10-09-01-0004

doi:10.4271/10-09-01-0004

NVH Performance of Permanent Magnet Synchronous Motors with Liquid Cooling System

Dario Barri,[1] Federico Soresini,[1] Federico Ballo,[1] Francescantonio Lucà,[1] Stefano Manzoni,[1] Massimiliano Gobbi,[1] and Giampiero Mastinu[1]

[1]Politecnico di Milano, Italy

Abstract

The aim of the article is to evaluate the effect of the cooling system on the NVH behavior of traction permanent magnets synchronous motors (PMSMs). An effective numerical method is proposed for modeling the fluid–structure interaction in the cooling system of PMSMs. A simplified physical prototype of a cooling jacket of a PMSM is realized by welding two concentric tubes with an internal cavity filled by coolant. A finite element model of the structure is realized. The coolant is modeled as an acoustic domain to account for the fluid–structure interaction in the cavity and a coupled acoustic–structural dynamic problem is solved. The model is validated by experimental modal tests conducted on the prototype of the cooling jacket both with and without the presence of coolant. The validated model is employed to quantify the effect of the cooling system on a real PMSM. The structure of a 10-poles, 12-slots electric machine is modeled by means of finite element method. The model includes the validated cooling jacket and the internal stator lamination and windings. Numerical vibroacoustic analyses have been performed at different operating conditions, either with or without modeling the coolant with the aim of quantifying its effect on the sound emission of the machine. Acoustic emission is generally increased when fluid coolant is present. For a PMSM, localized sound emission peaks appeared in the low-frequency range, up to 2000 Hz. A maximum increase of 44 dB was observed.

History

Received: 24 Jul 2024
Revised: 07 Oct 2024
Accepted: 21 Nov 2024
e-Available: 13 Jan 2025

Keywords

Cooling system, Electric motors, Fluid–structure interaction, NVH, Numerical model, Modal analysis, Sound emissions

Citation

Barri, D., Soresini, F., Ballo, F., Lucà, F. et al., "NVH Performance of Permanent Magnet Synchronous Motors with Liquid Cooling System," *SAE Int. J. Veh. Dyn., Stab., and NVH* 9(1):69-84, 2025, doi:10.4271/10-09-01-0004.

ISSN: 2380-2162
e-ISSN: 2380-2170

I. Introduction

The automotive industry is undergoing a period of transition from internal combustion engine vehicles (ICEVs) to electric vehicles (EVs). Comparing ICEVs to EVs, the influence of sound on dynamic discomfort is more pronounced in EVs than in ICEVs, due to the high tonal noise component emitted [1]. In addition, the masking effect by the engine noise is absent in EVs, this provides more prominence to the acoustic emission of the motor [2]. EVs' noise annoyance is dominated by high-frequency tones (above 1–2 kHz), generated by the electric motor, which are particularly annoying for the human ear [1, 3]. As a result, electric motors for traction applications play a major role in the total noise emission of EVs [4], introducing new noise, vibration, and harshness (NVH) issues for the designer [5, 6]. In recent years, many articles have addressed this topic and many reviews have been made [5, 6, 7, 8, 9, 10, 11, 12]. This fact emphasizes the importance of properly analyzing and studying the NVH topic applied to hybrid and EVs. Predicting noise radiation of electric motors (EMs) becomes an important step in the design phase to ensure a good level of comfort inside the vehicle.

Noise sources of an electric machine can be classified into three main categories, namely mechanical, aerodynamic, and electromagnetic [7]. The latter source, originated by electromagnetic forces acting on the stator, turns out to be the most important one [9, 10, 11]. For this reason, Song et al. [8], in their review paper focus on electromagnetic-induced vibrations, highlighted the multiphysics procedure needed to perform NVH analysis of EMs. A similar procedure is applied by Fang, who performed a complete vibroacoustic characterization of a permanent magnet synchronous motor (PMSM) of an electric vehicle by including the gearbox and current harmonics in the analysis [10]. Köpf and Berkemer [13] presented a multiphysics simulation approach for the calculation of NVH behavior of a PMSM, they couple the electromagnetic forces with the structural modes of the motor to obtain the resulting velocities of the stator surface. Deng et al. [12], in their research, reported an overview about EM-NVH problems focusing on PMSM, a widely adopted configuration in the automotive industry [14].

EM-NVH modeling generally consists of three sequential steps: electromagnetic force calculation, structural modeling, and acoustic simulation [8, 13, 15, 16]. Electromagnetic models are employed to compute the magnetic flux density field on the stator of the electric machine and the induced mechanical forces applied to the structure. The calculated mechanical forces acting on the stator teeth are the input loads of finite element (FE) models that compute the structural response of the EM. According to the literature, two main approaches to map the electromagnetic domain onto the mechanical one can be identified, namely concentrated equivalent force and nodal force transfer methods [15, 17, 18, 19, 20]. In the first method, a single resultant force is applied on the tooth head surface [17, 18] while in the second the electromagnetic forces are mapped on the structural mesh by means of a nodal interpolation approach [15, 19, 20]. Vibrations occurring on the external surface of the motor are transferred to the surrounding air, producing noise. Sound propagation is modeled either with FE method (FEM) or boundary element method (BEM). Hou et al. [21] made use of FEM to perform a complete numerical vibroacoustic analysis, employing discretized force distribution at each stator tooth. A spherical domain of the surrounding air is meshed and modeled as an acoustic medium. In [22, 23], the authors focused on the computation of the far-field acoustic emission of EMs by means of BEM, in this way they reduced the computational effort by avoiding meshing the entire volume of air.

All the above-mentioned works do not consider the cooling system of the electric motor, thus neglecting its effect on the NVH performance. However EMs for automotive applications are increasingly settling on compact and lightweight designs, leading to high power density motor configurations. Such kind of designs require however efficient liquid cooling systems to keep temperatures within safety operational levels [24, 25]. High temperatures would be reached during motor operation, resulting in demagnetization of the magnet and loss of insulation efficiency. At this aim, many types of cooling heat transfer mechanisms are applied to electric traction motors. These include cooling jackets (CJ), spray cooling, and high-speed rotor shaft cooling [26]. CJ represent the most common and studied solutions, they usually exploit round, elliptical, or rectangular channel geometries arranged either along the axial or hoop direction [see Figure 1(a) and (b), respectively]. Other solutions may include stator spray cooling [Figure 1(c)] or internal cooling acting on the rotor shaft [Figure 1(d)].

According to the literature, most of the research works concentrate their efforts in modeling the thermal behavior of the cooling system in EMs [25, 26], whereas the effect on NVH performances is analyzed only in a single paper [27]. In the paper, the authors quantify the effect of the cooling system on the acoustic emission of an electric motor by measuring the radiated noise on a test bench both with and without the presence of coolant. They found that the presence of coolant increases the external surface velocities and consequently the noise emission of the motor. The topic of fluid–structure interaction has been extensively studied in the literature; however, no papers referring to the NVH modeling of the cooling system of EMs can be found.

An effective method to model the fluid–structure interaction is the numerical structural–acoustic coupling [28, 29, 30, 31], in which acoustic wave equations are employed to model the pressure propagation within the fluid domain interacting with the structure at the boundaries. In these simulations, the fluid is usually modeled with acoustic FEs. Several fluid–structure interaction problems can be found in applications where seismic

FIGURE 1 Electric motor cooling systems: (a) CJ with axial cooling channels, (b) CJ with spiral cooling channels, (c) stator spray cooling, (d) rotor shaft cooling.

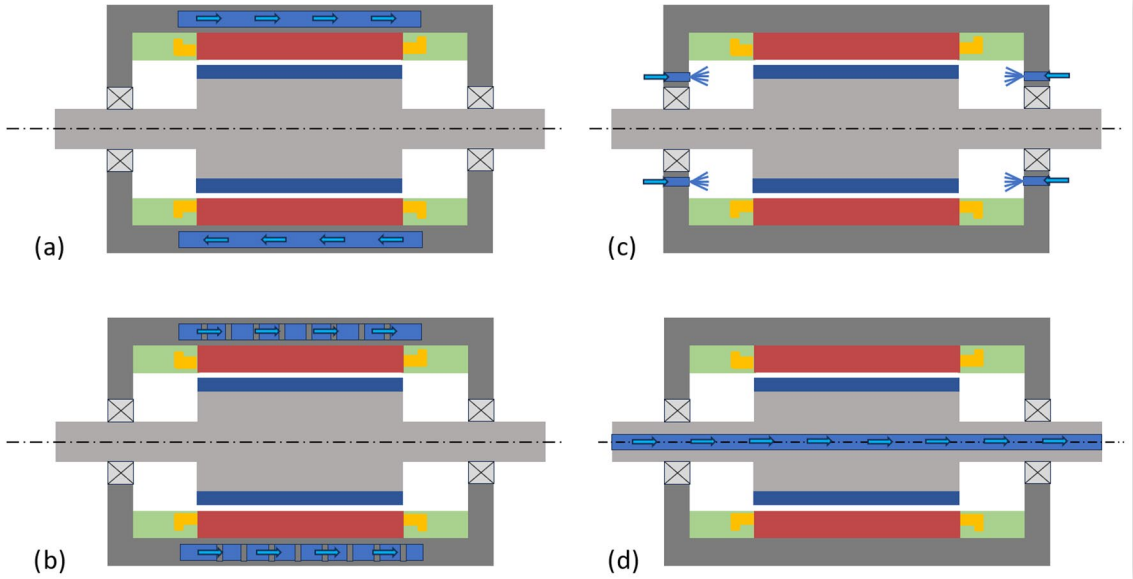

events are studied. As an example, in the work of Phan and Paolacci [28], a FE modeling approach based on structural–acoustic coupling is presented for the seismic response analysis of a steel storage tank. Further studies on acoustic wave propagation in fluid-filled pipes were conducted in [32, 33].

From a modeling point of view, no papers can be found in the literature to analyze the effect of the fluid–structure interaction introduced by the electric motor cooling system on its NVH behavior. This article aims to fill this gap proposing an effective numerical method for modeling the fluid–structure interaction in the cooling system of PMSMs to accurately estimate the acoustic pressure field radiated from the external surface of the stator. For this purpose, a simplified cylindrical structure (named *physical prototype* hereafter) equivalent to the cooling jacket of an electric motor is physically realized to validate the proposed numerical method. The physical prototype is made by two cylindrical structures with an internal cavity filled with fluid coolant. The simplification of the inner channels, with the absence of shaped ducts, facilitates the construction of the prototype by maintaining the structure representative of reality. In fact, working on a simplified structure allows for a more effective validation of the modeling approach, which is the main goal of the work. Experimental modal tests on the physical prototype are conducted to study the fluid–structure interaction and to validate the numerical method. Finally, the validated numerical method is employed to quantify the influence of the cooling system of the simplified prototype of cooling jacket on the NVH behavior of a Formula SAE PMSM [34].

The first part of the article describes the fluid–structure interaction modeling approach. Then, the physical prototype is modeled numerically and validated by experimental tests. The considered Formula SAE motor is described in Section III. Once the operating conditions are defined, the electromagnetic forces are calculated and applied to evaluate vibrations and noise emissions of the motor. The different numerical models and the entire process are presented. Finally, numerical results are shown and the cooling system's influence on the NVH behavior of the electric motor is discussed in Section IV.

II. Fluid–Structure Interaction on a Physical Prototype of the Cooling Jacket of a PMSM

A simplified physical prototype equivalent to the cooling jacket of an automotive electric motor was constructed. The prototype consists of two coaxial steel cylinders welded at both ends as shown in Figure 2. The two cylinders have a wall thickness of 3.5 mm. An internal enclosed cavity is left between the two cylindrical walls, which is filled with the fluid coolant as shown in Figure 2.

The geometry and dimensions of the physical prototype have been defined to be similar to those of typical cooling jacket structures employed in PMSMs for automotive applications [35]. Moreover, as the prototype was built in-house, the authors selected the most convenient materials (steel) and manufacturing procedure (welding of two concentric tubes) to realize the structure with an

FIGURE 2 Section of the physical prototype structure. The dots with numbers 1 to 6 indicate the position where accelerometers were placed during the experimental tests described in Section II-B.

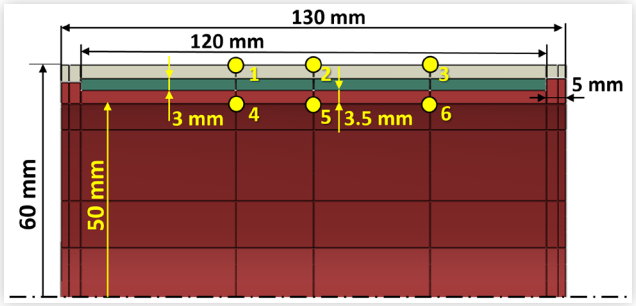

internal cavity. Finally, the shape of the internal cavity has been significantly simplified by removing the cooling channels in place of a uniform cavity. In this way, the model validation turns out to be more effective.

A. Numerical Model

A dynamic, linear FE model of the physical prototype is realized with ABAQUS CAE®. The model includes the two coaxial steel tubes and the internal fluid volume as shown in Figure 2. The two cylinders are connected at the two end flanges through a surface-based "tie" constraint on an annular region of 2 mm to model the welded connection. Linear elastic constitutive law is employed to model the material of the two cylinders (mass density ρ = 7700 kg/m^3, Young's modulus E = 206 GPa, Poisson's coefficient ν = 0.26) and a constant structural damping r = 0.004 is applied to the material [36]. The two parts are discretized with a mesh of linear brick elements. The element size is taken as 1 mm following a mesh convergence study.

The adopted cooling fluid is a mixture composed of 50% of water and 50% of glycol, modeled as an acoustic domain with a mass density of 1100 kg/m^3 and a bulk modulus K = 3 GPa [37]. AC3D8 linear bricks and acoustic elements are used to discretize the fluid volume. The element size is taken as 1 mm following a mesh convergence study.

The fluid–structure interaction is modeled by a "tie" constraint assigned to the fluid/solid interface surfaces. In this way, the same displacement is enforced on both structural and acoustic domains at the interface surface.

The FE formulation of the coupled fluid–structure dynamic problem reads [32, 38, 39]

$$\begin{bmatrix} \mathbf{M} & 0 \\ \mathbf{M_c} & \mathbf{M_f} \end{bmatrix} \begin{Bmatrix} \ddot{\mathbf{u}} \\ \ddot{\mathbf{p}} \end{Bmatrix} + \begin{bmatrix} \tilde{\mathbf{K}} & \mathbf{K_c} \\ 0 & \mathbf{K_f} \end{bmatrix} \begin{Bmatrix} \mathbf{u} \\ \mathbf{p} \end{Bmatrix} = \begin{Bmatrix} \mathbf{F_s} \\ \mathbf{F_f} \end{Bmatrix} \quad \text{Eq. (1)}$$

where **u** and **p** are the nodal unknown displacement and sound pressure vectors of the structural and acoustic domain, respectively, **M** is the structural mass matrix, $\mathbf{M_c}$ is the mass coupling matrix, $\mathbf{M_f}$ the acoustic mass matrix, $\tilde{\mathbf{K}}$ is the stiffness matrix of the structure, $\mathbf{K_c}$ is the stiffness coupling matrix, $\mathbf{K_f}$ is the acoustic stiffness matrix while $\mathbf{F_s}$ and $\mathbf{F_f}$ are the vectors of nodal structural and acoustic forces, respectively. Equation 1 was used for both solving the eigenvalue and eigenvector problem and extracting the structure's frequency response functions (FRFs). It is worth emphasizing that the proposed modeling approach works for an enclosed cavity completely filled with coolant. Additionally, being the model based on linear elasticity, small deformations are assumed for the structure. For the fluid domain, small pressure fluctuations are assumed and volume losses are neglected, meaning that no dissipation is associated with pressure waves traveling inside the medium.

B. Experimental Validation

Experimental modal tests were conducted with the purpose of validating the numerical model of the physical prototype. The physical prototype was instrumented with a set of six Bruel & Kjaer 4508 70 g piezoelectric accelerometers placed on the structure surface as depicted in Figure 2. A first row of three accelerometers was placed on the outer surface of the structure and a second one was placed on the same line but on the inner surface, in order to analyze the outside–inside vibration transfer path.

The input excitation is provided by a PCB 086C03 impact hammer equipped with a steel tip to excite the structure in the widest possible frequency range.

Figure 3 shows the experimental setup, showing the impact hammer and the physical prototype equipped

FIGURE 3 Experimental hammer test setup.

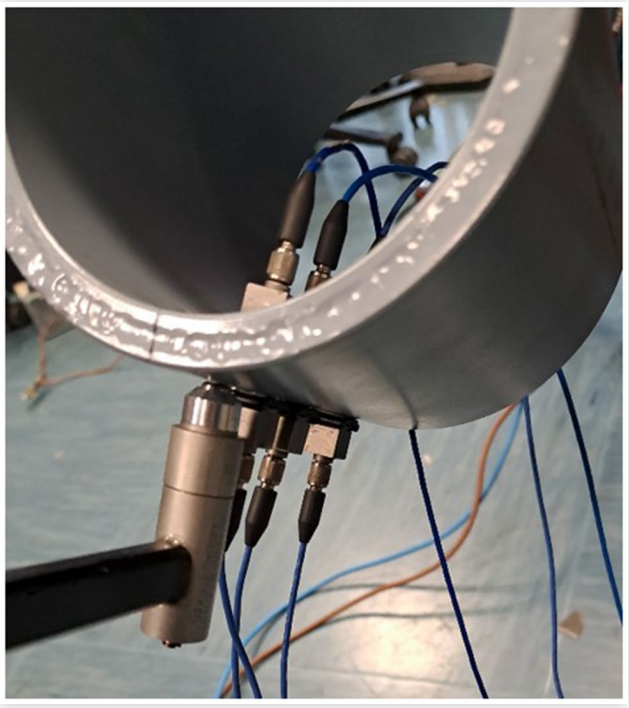

FIGURE 4 Numerical (black lines) and experimental (red lines) FRF amplitudes of the physical prototype without cooling fluid for two different input–output combinations. (a) Input 2—output 2. (b) Input 2—output 4. See Figure 2 for details related to the location of the points where input was applied and the response was measured.

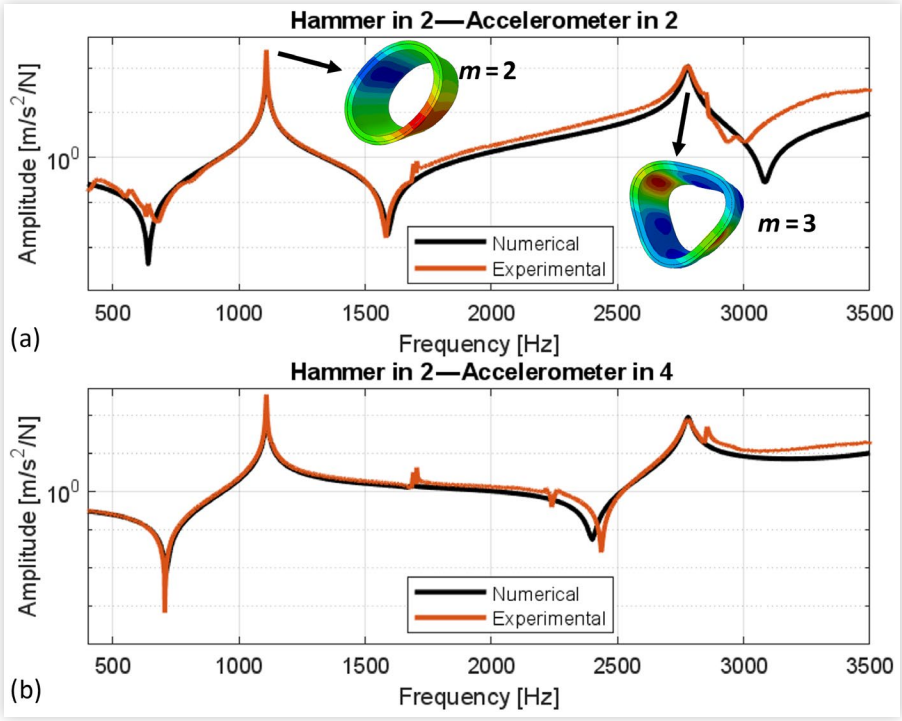

with accelerometers. The experimental validation is carried out by means of a hammer test in free–free conditions. Modal tests were done both with and without fluid coolant in the cavity.

The FRFs of the structure are extracted from the experimental measurements. Signals have been analyzed in the range 0–3500 Hz, a threshold of 20 dB attenuation on the power spectrum of the input hammer signal was considered to set the cutting frequency. Furthermore, the coherence function was analszed to check reliability of FRFs in the mentioned frequency range.

Figure 4 shows the comparison between simulated and experimental FRFs of the physical prototype without the presence of cooling in the cavity for two different input–output combinations. The plots show the presence of two main eigenmodes in the considered frequency range, namely a mode with two lobes located at a frequency of 1110 Hz and a mode with three lobes at a frequency of 2780 Hz. The presence of such kinds of eigenmodes is typical of cylindrical structures. The two modes are well-captured by numerical simulations [black lines of Figure 4(a) and (b)], with a maximum difference of 0.16% on the natural frequencies, see Table 1. The small variation between numerical and experimental eigenfrequencies demonstrates how the mass and modal stiffness of the model are correctly identified. A modal assurance criterion (MAC) [40] has been evaluated between numerical and experimental mode shapes obtaining a correlation higher than 99% for both the eigenmodes. The strong correlation obtained between numerical and experimental results confirms the accuracy of the numerical model of the welded structure.

TABLE 1 Comparison between numerical and experimental natural frequencies with and without cooling fluid in the cavity. The number of lobes is indicated by *m*.

		Modes			
	Natural freq.	*m* = 2	"a"	"b"	*m* = 3
Without water	Num. [Hz]	1100.0	/	/	2780.0
	Exp. [Hz]	1108.2	/	/	2776.1
	Difference %	0.16	/	/	0.14
With water	Num. [Hz]	941.3	1329.0	2015.0	2700.0
	Exp. [Hz]	954.5	1359.7	2119.0	2690.5
	Difference %	–1.4	–2.3	–5.2	0.35

A second set of tests involves the presence of the fluid coolant in the cavity. The coolant is filled from an external inlet at a pressure equal to 10^5 Pa. Figure 5 shows the numerical (black lines) and experimental (red lines) FRFs at the same locations for this structural configuration. In this case, it can be noticed that the natural frequencies of mode 2 and mode 3 are slightly reduced (from 1110 to 941 Hz for mode 2 and from 2780 to 2700 for mode 3) due to the effect of the additional mass of the coolant. The shifted modes have been compared with the ones without coolant by MAC. A correlation higher than 93% is reached, confirming that the modes remain the same. Besides mode 2 and mode 3, new vibration modes generated by the fluid–structure interaction can be identified. These modes are denoted as "a" and "b" in Figure 5 and mainly involve a vibration of the central cylindrical wall of the tubes. Mode "a" involves a three-lobed mode, while mode "b" involves a four-lobed mode. As shown in Figure 5, the numerical model correctly replicates all the additional peaks induced by the fluid–structural coupling [27]. In terms of natural frequencies, the difference between numerical and experimental frequencies is between 1 and 2% (see Table 1), with the exception of the peak located at 2 kHz, which features a slightly higher difference (i.e., 5%). Referring to the amplitude of the main peaks, a small variation is also noted here, reaching its maximum on the first ovalization mode around 20%. This value is considered reasonable since the comparison is made between 2 FRFs over a wide frequency range.

III. Effect of Cooling System on NVH of an Automotive PMSM

In this section the numerical method described and validated in Section II is employed to quantify the effect of the cooling system on NVH of PMSM for automotive application.

The acoustic emission of the motor is simulated both with and without coolant and results are compared. The electric motor under development is adapted from the PMSM of a Formula student electric race vehicle analyzed in [34]. The motor features a 10-poles, 12-slots architecture with poles arranged in spoke configuration. The external stator diameter and the axial stack length have been adjusted respectively to 100 and 80 mm in order to fit into the concentric tube cooling jacket described in Section II-B.

The motor has a maximum speed of 16,000 RPM and it exhibits constant torque–speed profile over the whole speed range. The main technical specifications are summarized in Table 2. An electromagnetic model of the PMSM is built by means of Motor-CAD® simulation software. Figure 6 depicts the cross section of the electromagnetic model of the motor along with a detail of the windings arrangement. Figure 7 shows the back electromotive force (EMF) waveforms computed by the model over an electrical period at 8000 RPM. Despite the slight

FIGURE 5 Experimental hammer test with cooling fluid (a) co-located FRF, (b) non co-located FRF.

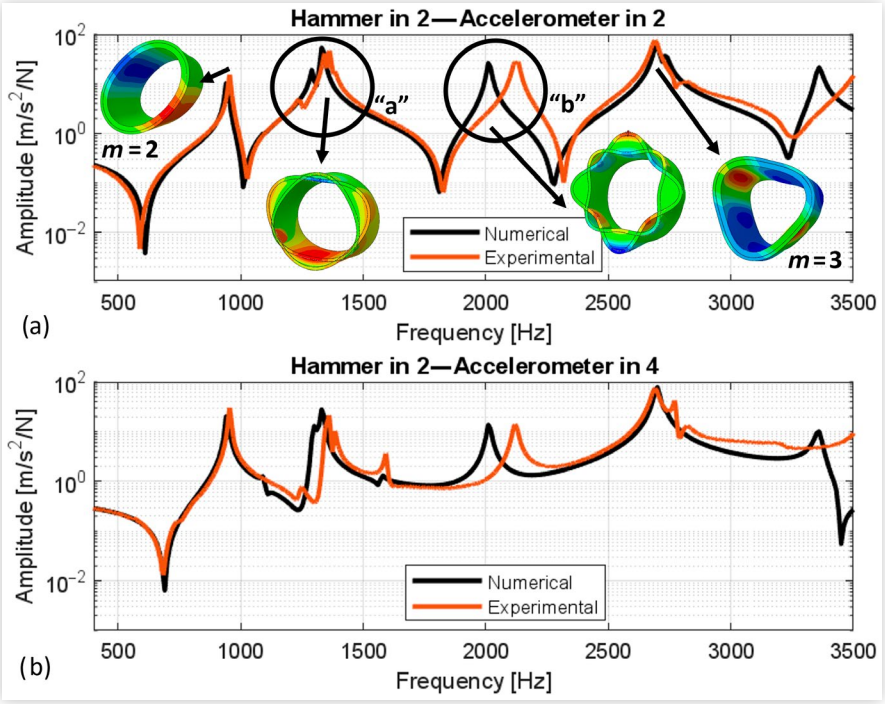

TABLE 2 Key motor parameters.

Stator outer diameter	*dext*	100 mm
Stator bore	*sb*	53 mm
Stator lamination thickness	*yt*	0.1 mm
Tooth width	*tw*	7.5 mm
Slot depth	*Sd*	16 mm
Slot opening	*So*	2.77 mm
Magnet thickness	*Mt*	5.5 mm
Magnet depth	*Md*	13.5 mm
Airgap	*Ag*	0.5 mm
Stack length	*le*	80 mm
End winding length	*ewl*	12 mm
Number of turns	*Nturns*	12
Number of strands in hand	N_s	13
Copper slot fill	*Csf*	0.40
Wire diameter	*dwire*	0.538 mm
Copper diameter	*dcu*	0.483 mm
Speed max	RPM_{max}	16,000 RPM
Rated voltage	*V*	510 V

geometrical modification introduced with respect to the motor from [34], the obtained quantities are consistent with those reported in the reference.

A. Electromagnetic Forces

A constant torque equal to 12 Nm is applied at the output shaft of the PMSM and radial and tangential force densities are computed at different revolution speeds. Figure 8 shows the time/space order spectrum of the radial electromagnetic force density computed at 8000 RPM and 50 A of peak current with an output torque of 12 Nm. This operating point is a representative continuous condition for the analyzed electric motor. Harmonic time orders are calculated with respect to the fundamental electric frequency of the machine. The electromagnetic force harmonic content shows that the main contribution is given by time order 2 harmonics, followed by time orders 4 and 6, respectively.

Figure 9 shows the tooth lumped radial [Figure 9(a)] and tangential [Figure 9(b)] force waveforms over an electric cycle.

FIGURE 6 Motor cross section and slot windings.

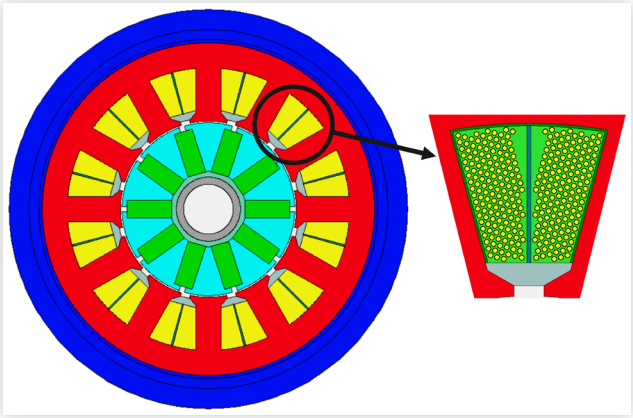

FIGURE 7 Back EMF waveforms at 8000 RPM.

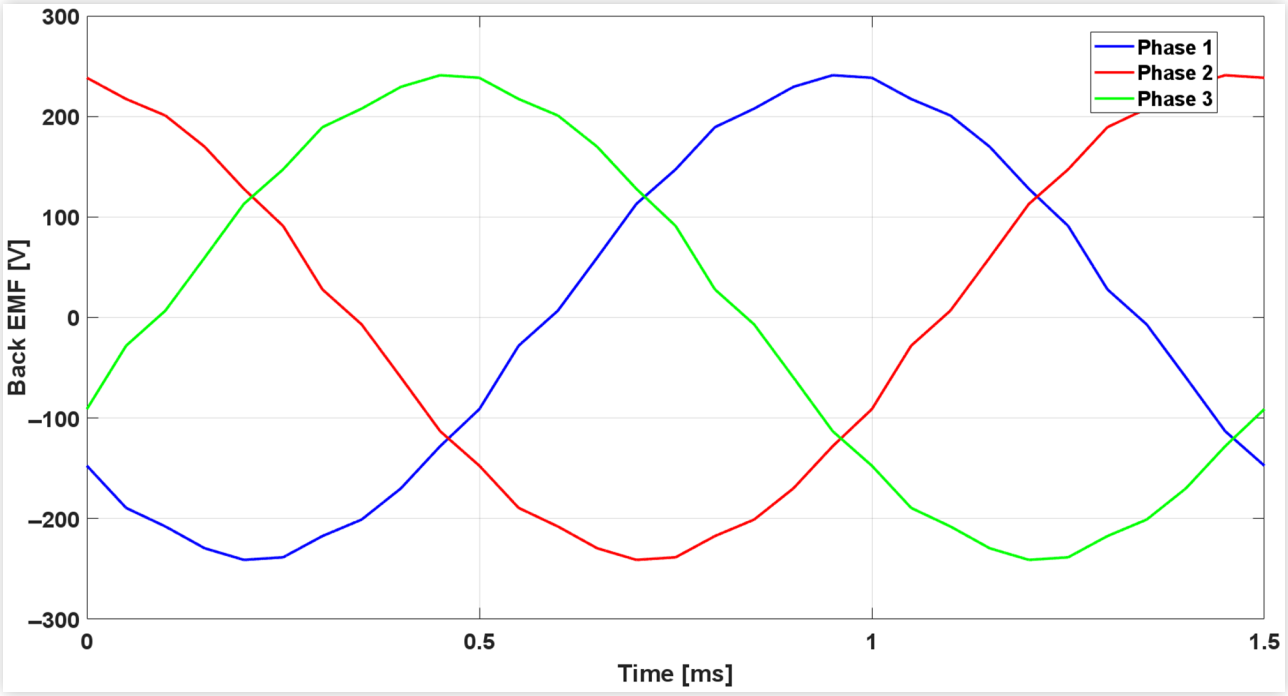

FIGURE 8 Radial force density FFT frequency domain 2D.

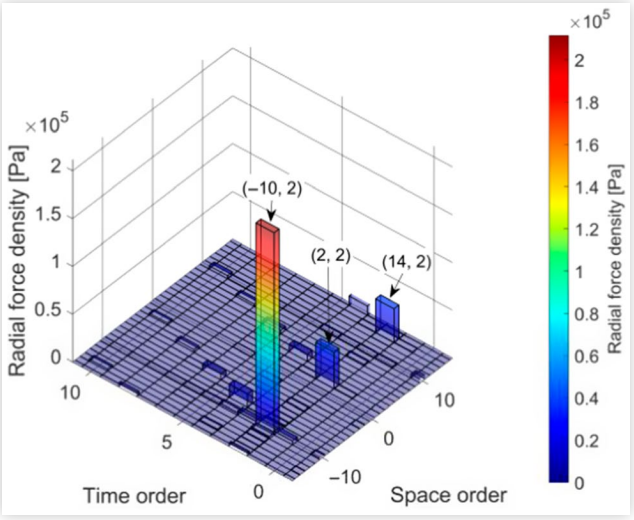

B. Motor Structural Model

FE approach is employed to model the structural response of the PMSM. The FE model of the motor includes three main parts, namely cooling jacket (described in Section II-A), stator lamination, and slot insulation with copper windings (see Figure 10).

1. *Stator lamination*: The stator lamination is realized by stacking a sequence of 0.1 mm metal sheets to reduce eddy current losses in the stator core [41]. Each metal sheet is covered by an insulating varnish [42], materials' physical properties are reported in Table 3. Such a kind of structure is generally modeled by orthotropic material parameters [43], specifically in this article the stator is modeled by a transversely isotropic material. The equivalent engineering constants are computed by means of the rule of mixtures as suggested by [44]. In the transverse plane (i.e., XY plane in Figure 10), the two phases are assumed to be arranged in parallel and the equivalent material constants read

$$E_x = E_y = E_{steel} \cdot v_{steel} + E_{varn} \cdot v_{varn} \quad \text{Eq. (2)}$$

$$G_{xy} = G_{steel} \cdot v_{steel} + G_{varn} \cdot v_{varn} \quad \text{Eq. (3)}$$

$$v_{xy} = \frac{E_x}{2 \cdot G_{xy}} - 1 \quad \text{Eq. (4)}$$

where $E_{steel/varn}$, $G_{steel/varn}$, and $v_{steel/varn}$ are the two phases, respectively.

Along the motor axis (Z axis in Figure 10), the equivalent Young's modulus and Poisson's ratios are calculated by assuming the two phases arranged in series

$$E_z = \frac{E_{steel} \cdot E_{varn}}{v_{steel} \cdot E_{varn} + v_{varn} \cdot E_{steel}} \quad \text{Eq. (5)}$$

$$v_{xz} = v_{yz} = \frac{v_{steel} \cdot v_{varn}}{v_{steel} \cdot v_{varn} + v_{varn} \cdot v_{steel}} \quad \text{Eq. (6)}$$

FIGURE 9 Lumped tooth forces at 12 Nm, 8000 RPM. (a) Radial force waveforms. (b) Tangential force waveforms.

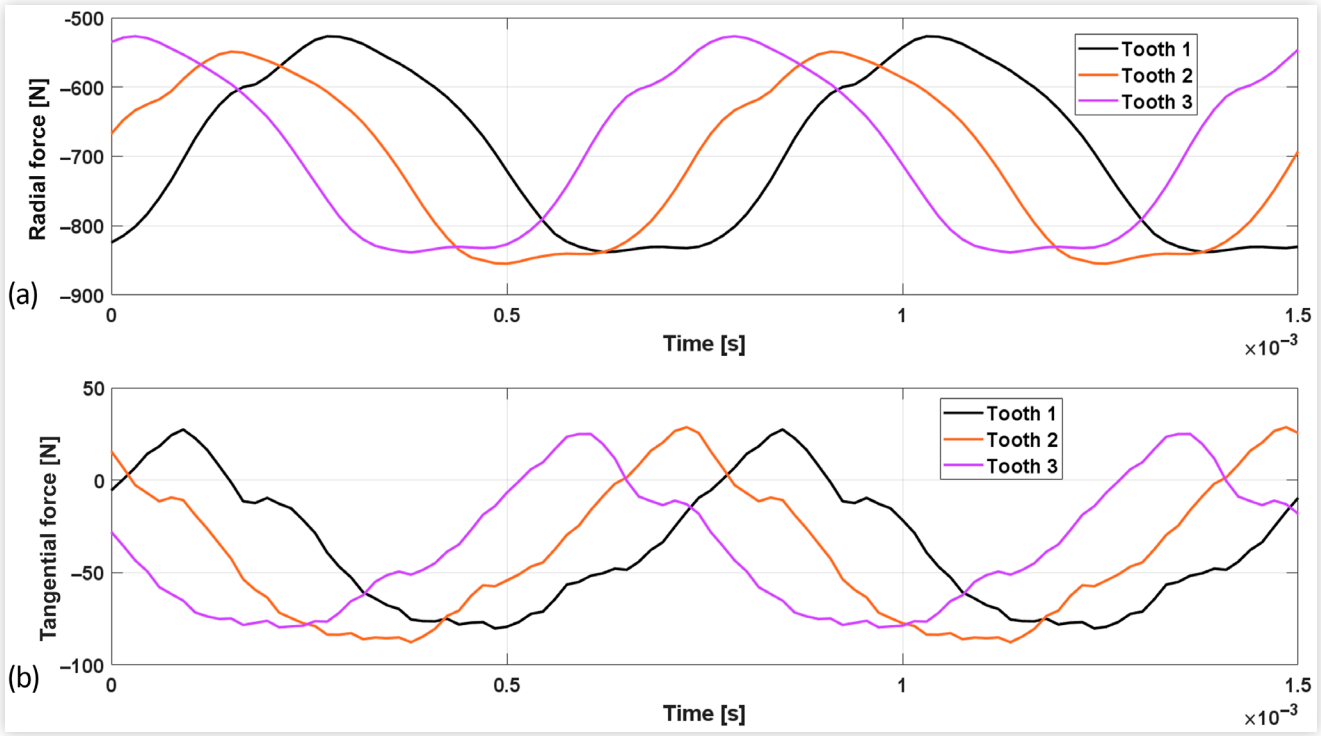

TABLE 3 Stator core materials physical properties.

	Description	Steel	Varnishing	Resin	Copper	Units
E	Young's modulus	185	1	10	115	GPa
G	Shear modulus	71.15	0.37	3.7	43.2	GPa
ν	Poisson's ratio	0.3	0.35	0.35	0.33	
ρ	Density	7650	2350	2350	8960	kg/m^3
v	Volume fraction	0.96	0.04			

where $\nu_{steel/varn}$ are the Poisson's ratios of the two phases.

For the shear moduli G_{xz}, G_{yz}, a mixed series–parallel phase arrangement is assumed as proposed by [44]

$$G_{xz} = G_{yz} = \frac{E_{mix}}{2\left(1+\nu_{xz}\right)} \quad \text{Eq. (7)}$$

where

$$E_{mix} = \frac{h_1 \cdot E_{steel} + h_2 \cdot E_{varn}}{h_1 + h_2} \quad \text{Eq. (8)}$$

$$h_1 = v_{steel} \cdot \left(q + E_{varn}\right) \quad \text{Eq. (9)}$$

$$h_2 = v_{varn} \cdot \left(q + E_{steel}\right) \quad \text{Eq. (10)}$$

and

$$q = v_{steel} \cdot \frac{E_{steel}}{2\left(1+\nu_{steel}\right)} + v_{varn} \cdot \frac{E_{varn}}{2\left(1+\nu_{varn}\right)} \quad \text{Eq. (11)}$$

2. *Slot insulation and copper windings*: The polymeric insulation is modeled with a single, linear elastic solid filling the stator slots. The polymer insulation is rigidly connected to the stator lamination at the interface surfaces. To account for the effective volume in the slots, the elastic modulus of the polymer insulation is scaled according to the effective insulation slot fill η_{ins} as

$$E_{ins} = E_{resin} \cdot \eta_{ins} \quad \text{Eq. (12)}$$

FIGURE 10 3D FE motor physical model.

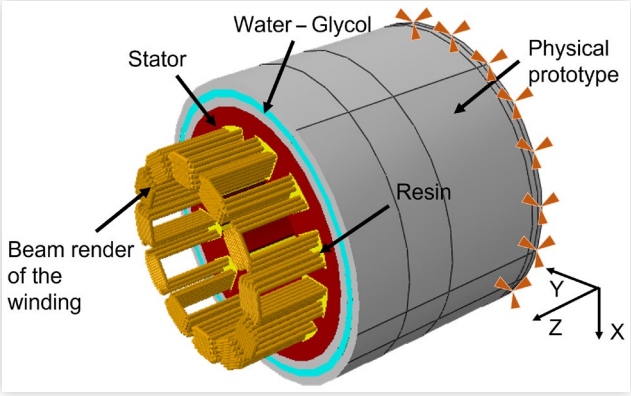

with

$$\eta_{ins} = \frac{V_{ins}}{V_{slot}} = 0.8 \quad \text{Eq. (13)}$$

where E_{ins} and V_{ins} are the Young's modulus and volume of the polymer insulation in the slot, while V_{slot} is the entire volume of the slot.

A constant structural damping equal to 0.05 has been assigned to the polymer insulation to model internal material dissipation [36].

One-dimensional beam elements are employed to model the copper windings. Each winding turn is discretized by a mesh of quadratic beam elements acting as reinforcements embedded in the polymer insulation material as shown in Figure 10. A generalized cross section has been assigned to the beam elements, in this way the winding cross-sectional area and moment of inertia can be independently defined. The cross-sectional area of each turn reads

$$A_{turn} = N_s \cdot \frac{\pi d_{cu}^2}{4} \quad \text{Eq. (14)}$$

while the moment of inertia of each turn is calculated assuming no interaction among the single copper conductors composing the turn and reads

$$I_{turn} = \sum_{i=1}^{N_s} \pi \frac{d_{cu}^4}{64} \quad \text{Eq. (15)}$$

The computed material properties of the laminated stator are reported in Table 4.

A constant structural damping equal to 0.004 has been assigned to the stator lamination to account for dynamic viscous effects [36].

C. Structural Dynamic Simulation

The stator is discretized with C3D8R linear brick elements with typical dimension equal to 1.5 mm. The stator is connected to the physical prototype by a "tie" constraint. From the radial (Figure 8) and tangential force spectrum the tooth resultant forces have been calculated and applied by means of a uniform pressure distribution on the tooth head, a similar approach is presented in [45, 46]. The main time orders of the tooth resultant forces (2, 4, 6) calculated in Section III-A have been selectively considered for the vibroacoustic analyses.

TABLE 4 Equivalent computed stator core transversely isotropic properties, based on equations from 2 to 11.

	Description	Value	Units
$E_X = E_Y$	Young's modulus: X, Y direction	177.6	GPa
E_Z	Young's modulus: Z direction	22.1	GPa
νXY	Poisson coefficient: XY plane	0.3	
$\nu XZ = \nu ZY$	Poisson coefficient: XZ, ZY plane	0.3017	
GXY	Shear modulus: XY plane	68.32	GPa
$GXZ = GZY$	Shear modulus: XZ, ZY plane	61.72	GPa

Additionally, the effect of rotor unbalances was neglected for two main reasons

- Their effect is associated with mechanical noise, confined in the low-frequency range, generally less stressful for the human ear [9]
- Rotor unbalances are generally associated to the structure-borne noise contributions, whereas the focus of the article is to study the effect of the cooling system on the vibration of the external surface of the stator and the related (air-borne) noise radiation [47].

The motor is constrained at the rear flange of the stator as shown in Figure 10. A steady-state modal dynamic (SSD) analysis is performed by means of Abaqus Standard®. The SSD analysis is performed approximating a slow ramp, so that all transient effects are negligible. In this way, each frequency step is considered under steady-state conditions. At first the structure eigenmodes up to a frequency of 100 kHz are extracted, then the steady-state forced vibration is reconstructed by a modal superposition approach. When the fluid coolant is included in the simulation, the number of eigenmodes found in the same frequency range increases significantly. This increment is explained by the additional dynamic modes introduced by the fluid mass and leads to a significant increase in the computational effort needed to solve the problem. For this reason, the eigenmodes extraction has been limited to 70 kHz for the case with fluid coolant. This simplification has been checked by comparing the results with those coming from a steady-state dynamic simulation performed by considering the physical degrees of freedom in place of the modal superposition approach. The analysis has been performed considering a rotational speed ranging from 2000 to 16,000 RPM and a constant output torque of 12 Nm. As shown in Figure 8, the main harmonic contributions of the electromagnetic forces are given by time orders 2, 4, and 6, therefore the structural dynamics are solved considering only these harmonic components.

D. Acoustic Model

A cylindrical volume of the surrounding air is realized and meshed with AC3D4 4-node linear acoustic tetrahedral elements as shown in Figure 11. The size of the finite element and the volume of the air domain affect the frequency range in which numerical results are reliable [48]. The element size affects the maximum frequency f_{max} that can be captured by the numerical simulation as reported in [48]

$$f_{max} \simeq \frac{c}{6 \cdot L_{max}} \qquad \text{Eq. (16)}$$

where $c = \sqrt{K/\rho}$ is the speed of sound in the acoustic medium, K is the bulk modulus, ρ is the mass density, and L_{max} is the maximum element internodal distance. Equation 16 suggests that as the vibration frequency increases, the maximum element size should be reduced.

The minimum frequency f_{min}, on the other hand, depends on the minimum distance r_{min} between the boundaries of the air volume and the radiating surface [48]

$$f_{min} \simeq \frac{c}{3 \cdot r_{min}} \qquad \text{Eq. (17)}$$

FIGURE 11 Air domain and microphones.

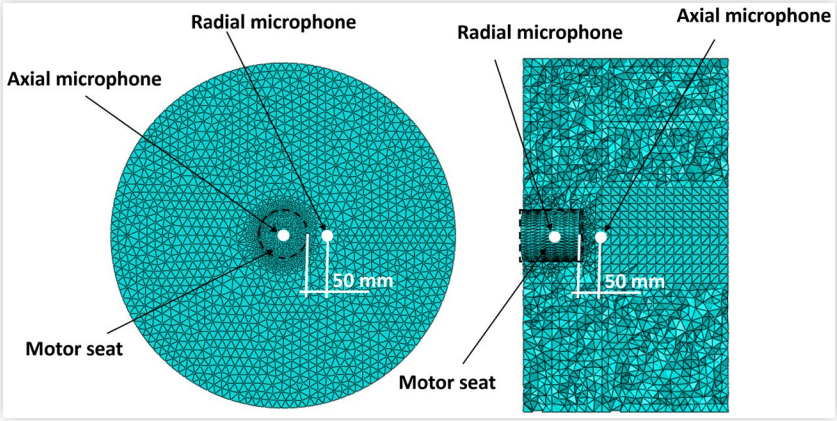

FIGURE 12 Comparison of vibration results with and without coolant.

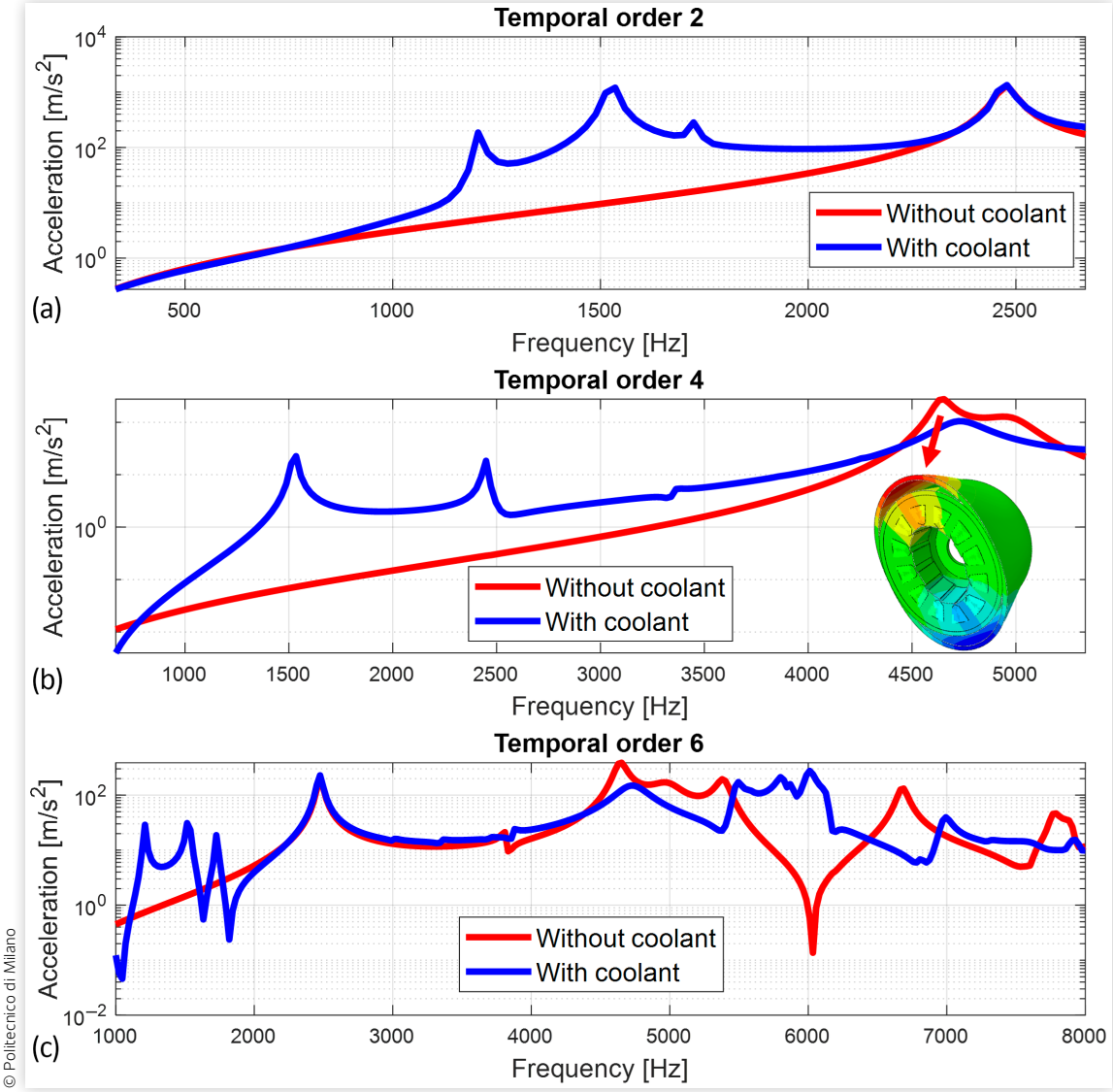

which means that the lower the frequency, the larger the air volume to be considered.

In this case, a maximum element size of 7 mm has been employed for the analysis, with a minimum distance between the boundaries and the radiating surface of 341 mm, which allows accurately capturing sound pressure vibrations in a frequency range between 333 and 8000 Hz.

The air–structure interaction is studied by applying the submodeling technique [48]. This improves computational efficiency because the structural and acoustic simulations are simulated independently. The interface surface in the acoustic domain takes as input the external nodal velocity given by the vibration of the electric motor, so as to simulate the propagation of sound in the acoustic domain. Non-reflecting surface boundary conditions have been enforced on the boundary of the acoustic domain. In this way no backward reflection is generated when the sound pressure wave hits the boundary, mimicking an infinitely extended acoustic domain.

IV. Results and Discussion

Structural and acoustic simulations have been performed both with and without the presence of coolant in the cooling jacket. Figure 12 shows the simulated radial acceleration at point 2 of Figure 2 for time orders 2, 4, and 6, respectively. Simulations refer to a rotational speed that ranges from 2000 to 16,000 RPM. In the plots, the red lines are obtained without the presence of coolant in the cooling jacket, while the black ones refer to the case in which coolant is present.

Without cooling fluid, the first excited structural mode is located around 2500 Hz [Figure 12(a)] and involves a bending deformation of the whole motor. This mode is excited only by order 2 and order 6 harmonics [Figure 12(a) and (c)].

When the coolant is added to the cavity, additional modes at lower frequencies appear (1200, 1530, and 1700 Hz, respectively), which are caused by the fluid–structure interaction in the cavity of the cooling jacket and in particular by the pressure waves that propagate inside the fluid domain and interact with the wall surfaces of the cavity. The main structural modes of the motor (i.e., at 2500 Hz and in the range 4500–5000 Hz) are less sensitive to the presence of the coolant, as can be observed in Figure 12.

The sound pressure amplitude p in the air domain is computed by the acoustic model and the sound pressure level (SPL) can be calculated as

$$SPL_{dB} = 20 \cdot \log_{10}\left(\frac{p}{p_{ref}}\right) \qquad \text{Eq. (18)}$$

where p_{ref} is the reference pressure equal to $2 \cdot 10^{-5}$ Pa [49].

Results of the acoustic simulations with and without the cooling fluid are compared in the spectrograms of Figures 13 and 14, where the sound pressure levels are simulated at two different points located at a distance of 50 mm from the motor surface in radial and axial direction, respectively (see Figure 11). The spectrograms show the acoustic emission evolution in a speed range from 2000 to 16,000 RPM for the three main identified harmonic orders (i.e., time orders 2, 4, and 6).

For the radial microphone, the maximum sound emission occurs around 2500 Hz, with an emission of 126.6 dB(A) for the case with coolant and 125.7 dB(A) in case no coolant is present [see Figure 13(a) and (b), respectively]. This peak is mainly caused by the bending structural vibration mode excited by order 2 harmonic. Other peaks can be noticed between 4500 and 5000 Hz on orders 4 and 6, which are due to the excitation of an eigenmode with two lobes of the motor [Figure 12(b)].

When the fluid coolant is added, three localized peaks can be seen on order 2 harmonic excitation around 1200, 1530, and 1700 Hz, respectively, which are due to the new structural modes introduced by the fluid–structure interaction clearly evident in Figure 12(a). Considering each individual order, a maximum increase in sound emission of 33 dB is achieved for the first time order, while for the second and third time orders an increase of 44 and 24 dB in the low-frequency range is achieved, respectively.

In axial direction (Figure 14), lower sound emission levels are computed with respect to the radial one. Even in this case, similar trends can be identified. The general increase in acoustic emission is essentially related to the generation of new structural modes by the fluid–structure interaction. These are excited by electromagnetic forces generating additional noise contributions.

The results are consistent with the experimental data collected in [27], in fact it is confirmed that the addition of the cooling fluid has a negative effect on the acoustic radiation of the electrical machine, since it increases the average sound emission levels in the electrical machine's working range. Since all high-performance electrical machines are equipped with a cooling system, it is

FIGURE 13 Radial microphone spectrograms without cooling (a) and with cooling (b).

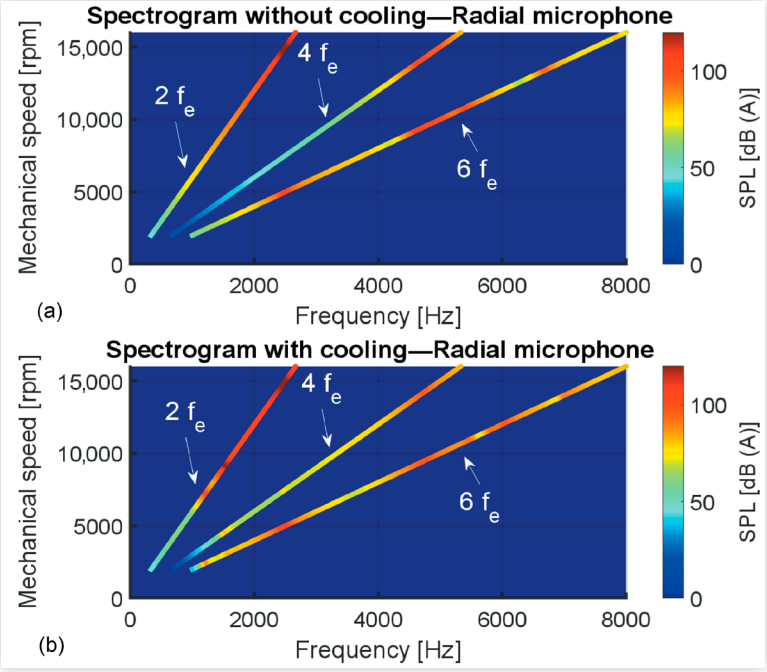

FIGURE 14 Axial microphone spectrograms without cooling (a) and with cooling (b).

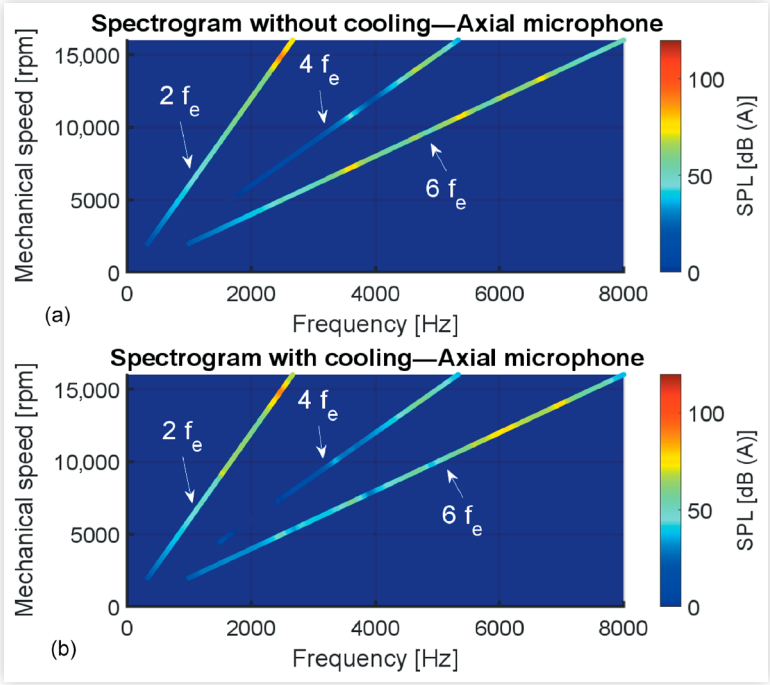

therefore essential to correctly model the fluid–structure interaction generated within the cooling channels, as proposed in this article.

The article provides a first contribution toward accurate modeling of the effect of the cooling system on the vibration of the external stator of an electric motor. Actual CJ may exhibit much higher complexity, both in terms of structural geometry and of shapes of the cooling channels. However, the numerical approach we propose is general and can be applied also to more complex and realistic designs.

V. Conclusions

The article deals with the effect of liquid cooling systems on NVH behavior of PMSMs for automotive applications. A method to compute the acoustic behavior of PMSMs by accounting for the presence of the coolant has been proposed. A simplified physical prototype of a PMSM cooling jacket was constructed by welding two concentric steel tubes and leaving an internal cavity to be filled with coolant. Experimental modal tests on the physical prototype have been conducted both with and without the presence of coolant in the cavity to validate the numerical model. The FE model of the cooling jacket was realized considering the coolant inside the cavity as an acoustic medium. The coupled structural–acoustic problem was solved to account for the fluid–structure interaction at the boundaries of the cavity.

The model was able to replicate all the additional structural modes that arise when the cavity is filled by coolant. The validated model was used to numerically assess the effect of cooling system on NVH of a PMSM for automotive application. A 10-pole, 12-slots PMSM employed on a race electric vehicle was used as a case study.

A physical model of the laminated stator and cooling jacket was realized with Abaqus so as to evaluate the dynamic forced vibration and acoustic emissions. The comparative simulations were performed both with and without the presence of coolant in the jacket channels, in order to validate the proposed methodology. Numerical results showed that the presence of cooling fluid in the cavity introduces additional vibration modes at low frequencies, caused by the interaction between the pressure waves traveling inside the fluid domain and the jacket surfaces.

Acoustic simulations highlighted a general increase in the acoustic emission of the machine when fluid coolant is introduced in the cavity. Additionally, when the coolant is present, localized sound emission peaks appeared in the low-frequency range up to about 2000 Hz. These peaks are excited by the coupled fluid–structural vibration modes. A maximum increase in noise emission up to 44 dB was observed in this frequency band.

This article shows how the presence of coolant in EMs leads to increased acoustic emission. This phenomenon is generated by the fluid–structure interaction, which must be properly modeled by an acoustic domain in FEM models. A validated simple modeling procedure is reported in the article. Since almost all PMSMs are

fluid-cooled, the fluid–structural interaction should be always modeled in NVH analysis of EMs. On the basis of the proposed method and on the results obtained, future studies on the NVH of EMs will be able to properly consider the contribution of the cooling system in the noise emission of EMs. The presented method could be included during future motor design and optimization processes.

The next steps of this research will be to verify fluid–structure modeling even on more complex cooling jacket geometries, such as spiral cooling channel structures commonly present in the automotive sector.

Acknowledgements

This study was carried out within the MOST Sustainable Mobility Center and received funding from the European Union Next-GenerationEU (PIANO NAZIONALE DI RIPRESA E RESILIENZA (PNRR), MISSIONE 4 COMPONENTE 2, INVESTIMENTO 1.4, D.D. 1033 17/06/2022, CN00000023). This manuscript reflects only the authors' views and opinions, neither the European Union nor the European Commission can be considered responsible for them.

Contact Information

Gianpiero Mastinu, corresponding author
Politecnico di Milano
via Privata Giuseppe La Masa 1
20156 Milano, Italy
gianpiero.mastinu@polimi.it

References

1. Wang, X., Osvalder, A., and Höstmad, P., "Influence of Sound and Vibration on Perceived Overall Ride Comfort—A Comparison between an Electric Vehicle and a Combustion Engine Vehicle," *SAE Int. J. Veh. Dyn., Stab., and NVH* 7, no. 2 (2023): 153-171, doi:https://doi.org/10.4271/10-07-02-0010.
2. Mahadevan, U., Kumar, V., and Sambharam, T., "A Multiphysics Approach for NVH Analysis of PMSM Traction Motor," SAE Technical Paper 2021-26-0520 (2021), doi:https://doi.org/10.4271/2021-26-0520.
3. Lennström, D., Johnsson, R., Nykänen, A., and Ågren, A., "Determination of Radiated Sound Power from an Electric Rear Axle Drive In-Situ and its Contribution to Interior Noise," *SAE Int. J. Passeng. Cars - Mech. Syst.* 6, no. 3 (2013): 1554-1563, doi:https://doi.org/10.4271/2013-01-9120.
4. Padavala, P., Inavolu, N., Thaveedu, J., and Medisetti, J., "Challenges in Noise Refinement of a Pure Electric Passenger Vehicle," *SAE Int. J. Veh. Dyn., Stab., and NVH* 5, no. 1 (2021): 45-64, doi:https://doi.org/10.4271/10-05-01-0004.
5. Hazra, S. and Reddy, J., "An Aspect of Noise, Vibration, and Harshness Issues in Electric Vehicles," *SAE Int. J. Veh. Dyn., Stab., and NVH* 6, no. 1 (2022): 23-33, doi:https://doi.org/10.4271/10-06-01-0002.
6. Soresini, F., Barri, D., Ballo, F., Gobbi, M. et al., "Noise and Vibration Modelling of Permanent Magnet Synchronous Motors: A Review," *IEEE Transactions on Transportation Electrification* (2024): 1-18, doi:https://doi.org/10.1109/TTE.2024.3365151.
7. Qin, Y., Tang, X., Jia, T., Duan, Z. et al., "Noise and Vibration Suppression in Hybrid Electric Vehicles: State of the Art and Challenges," *Renewable and Sustainable Energy Reviews* 124 (2020): 109782.
8. Song, P., Li, W., Mukundan, S., and Kar, N.C., "An Overview of Noise-Vibration-Harshness Analysis for Induction Machines and Permanent Magnet Synchronous Machines," in *2020 10th International Electric Drives Production Conference (EDPC)*, Ludwigsburg, Germany, 2020, https://doi.org/10.1109/EDPC51184.2020.9388189, IEEE.
9. Remus, N., Toulabi, M.S., Mukundan, S., Dhulipati, H. et al., "Electromagnetic Noise and Vibration in PMSM and Their Sources: An Overview," in *2020 IEEE Canadian Conference on Electrical and Computer Engineering (CCECE)*, London, ON, Canada, 2020, 1-4, IEEE.
10. Fang, Y. and Zhang, T., "Vibroacoustic Characterization of a Permanent Magnet Synchronous Motor Powertrain for Electric Vehicles," *IEEE Transactions on Energy Conversion* 33, no. 1 (2017): 272-280.
11. Rahmani, M., Darabi, A., and Deylami, F.P., "Impact of the Stator Coil Pitch on Acoustic Noise and Vibration of Squirrel Cage Induction Motors," *IEEE Transactions on Energy Conversion* 38, no. 4 (2023): 2344-2352.
12. Deng, W. and Zuo, S., "Electromagnetic Vibration and Noise of the Permanent-Magnet Synchronous Motors for Electric Vehicles: An Overview," *IEEE Transactions on Transportation Electrification* 5 (2019): 59-70, doi:https://doi.org/10.1109/TTE.2018.2875481.
13. Köpf, C. and Berkemer, J., "Noise, Vibration, and Harshness Simulation of a Synchronous Motor with Focus on the Influence of Eccentricity on the Electromagnetic Forces," *SAE Int. J. Veh. Dyn., Stab., and NVH* 6, no. 2 (2022): 101-113, doi:https://doi.org/10.4271/10-06-02-0007.
14. Gobbi, M., Sattar, A., Palazzetti, R., and Mastinu, G., "Traction Motors for Electric Vehicles: Maximization of Mechanical Efficiency: A Review," *Applied Energy* 357 (2024): 122496, doi:https://doi.org/10.1016/j.apenergy.2023.122496.
15. Lin, F., Zuo, S., Deng, W., and Wu, S., "Modeling and Analysis of Electro-Magnetic Force, Vibration, and Noise in Permanent-Magnet Synchronous Motor Considering

Current Harmonics," *IEEE Transactions on Industrial Electronics* 63, no. 12 (2016): 7455-7466.

16. Ballo, F., Gobbi, M., Mastinu, G., and Palazzetti, R., "Noise and Vibration of Permanent Magnet Synchronous Electric Motors: A Simplified Analytical Model," *IEEE Transactions on Transportation Electrification* 9, no. 2 (2022): 2486-2496.
17. Fang, H., Li, D., Qu, R., and Yan, P., "Modulation Effect of Slotted Structure on Vibration Response in Electrical Machines," *IEEE Transactions on Industrial Electronics* 66 (2019): 2998-3007, doi:https://doi.org/10.1109/TIE.2018.2847639.
18. Kim, J.H., Park, S.H., Ryu, J.Y., and Lim, M.S., "Comparative Study of Vibration on 10-Pole 12-Slot and 14-Pole 12-Slot PMSM Considering Tooth Modulation Effect," *IEEE Transactions on Industrial Electronics* 70, no. 4 (2022): 4007-4017, doi:https://doi.org/10.1109/TIE.2022.3181418.
19. Zuo, S., Lin, F., and Wu, X., "Noise Analysis, Calculation, and Reduction of External Rotor Permanent-Magnet Synchronous Motor," *IEEE Transactions on Industrial Electronics* 62 (2015): 6204-6212, doi:https://doi.org/10.1109/TIE.2015.2426135.
20. Ibrahim, I. and Lowther, D.A., "Effects of Stator Laminations on Acoustic Noise of Electrical Machines," in *2021 IEEE Energy Conversion Congress and Exposition (ECCE)*, Vancouver, BC, Canada, 2021, 3902-3908, IEEE, https://doi.org/10.1109/ECCE47101.2021.9595073.
21. Hou, P., Ge, B., Tao, D., Wang, Y. et al., "Coupling Analysis of Electromagnetic Vibration and Noise of FeCo-Based Permanent-Magnet Synchronous Motor," *Energies* 15 (2022): 3888, doi:https://doi.org/10.3390/en15113888.
22. Sathyan, S., Aydin, U., and Belahcen, A., "Acoustic Noise Computation of Electrical Motors Using the Boundary Element Method," *Energies* 13 (2020): 245, doi:https://doi.org/10.3390/en13010245.
23. Park, S., Kim, W., and Kim, S.I., "A Numerical Prediction Model for Vibration and Noise of Axial Flux Motors," *IEEE Transactions on Industrial Electronics* 61 (2014): 5757-5762, doi:https://doi.org/10.1109/TIE.2014.2300034.
24. Rehman, Z. and Seong, K., "Three-D Numerical Thermal Analysis of Electric Motor with Cooling Jacket," *Energies* 11, no. 1 (2018): 92, doi:https://doi.org/10.3390/en11010092.
25. Zhang, B., Qu, R., Fan, X., and Wang, J., "Thermal and Mechanical Optimization of Water Jacket of Permanent Magnet Synchronous Machines for EV Application," in *2015 IEEE International Electric Machines Drives Conference*, Coeur d'Alene, ID, 2015, 1329-1335, https://doi.org/10.1109/IEMDC.2015.7409234.
26. Gronwald, P.-O. and Kern, T.A., "Traction Motor Cooling Systems: A Literature Review and Comparative Study," *IEEE Transactions on Transportation Electrification* 7, no. 4 (2021): 2892-2913.
27. Schnell, M. and Gauterin, F., "Acoustic Effects of the Coolant Mass Flow of an Electric Machine of a Hybrid Drive Train," *Automotive and Engine Technology* 4 (2019): 189-193.
28. Phan, H.N. and Paolacci, F., "Fluid-Structure Interaction Problems: An Application to Anchored and Unanchored Steel Storage Tanks Subjected to Seismic Loadings," arXiv preprint arXiv:1805.00679, 2018.
29. Moshkelgosha, E., Askari, E., Jeong, K.H., and Shafiee, A.A., "Fluid-Structure Coupling of Concentric Double FGM Shells with Different Lengths," *Structural Engineering and Mechanics* 61 (2017): 231-244, doi:https://doi.org/10.12989/sem.2017.61.2.231.
30. Virella, J.C., Godoy, L.A., and Suárez, L.E., "Fundamental Modes of Tank-Liquid Systems under Horizontal Motions," *Engineering Structures* 28 (2006): 1450-1461, doi:https://doi.org/10.1016/j.engstruct.2005.12.016.
31. Virella, J.C., Prato, C.A., and Godoy, L.A., "Linear and Nonlinear 2D Finite Element Analysis of Sloshing Modes and Pressures in Rectangular Tanks Subject to Horizontal Harmonic Motions," *Journal of Sound and Vibration* 312 (2008): 442-460, doi:https://doi.org/10.1016/j.jsv.2007.07.088.
32. Hansson, P.-A. and Sandberg, O., "Dynamic Finite Element Analysis of Fluid-Filled Pipes," *Computer Methods in Applied Mechanics and Engineering* 190, no. 24-25 (2001): 3111-3120.
33. Abdullahi, M. and Oyadiji, S.O., "Acoustic Wave Propagation in Air-Filled Pipes Using Finite Element Analysis," *Applied Sciences (Switzerland)* 8 (2018): 1318, doi:https://doi.org/10.3390/app8081318.
34. Hu, X., Guo, H., Qian, H., Ding, X. et al., "Development of a High-Power-Density Motor for Formula Student Electric Race Car," in *IECON 2017 - 43rd Annual Conference of the IEEE Industrial Electronics Society*, Beijing, China, 2017.
35. Liang, P., Chai, F., Shen, K., and Liu, W., "Water Jacket and Slot Optimization of a Water-Cooling Permanent Magnet Synchronous In-Wheel Motor," *IEEE Transactions on Industry Applications* 57, no. 3 (2021): 2431-2439, doi:https://doi.org/10.1109/TIA.2021.3064779.
36. Orban, F., "Damping of Materials and Members in Structures," *Journal of Physics: Conference Series* 268 (2011): 012022, doi:https://doi.org/10.1088/1742-6596/268/1/012022.
37. George, J. and Sastry, N.V., "Densities, Dynamic Viscosities, Speeds of Sound, and Relative Permittivities for Water+ Alkanediols (Propane-1, 2- and-1, 3-Diol and Butane-1, 2-,-1, 3-,-1, 4-, and-2, 3-Diol) at Different Temperatures," *Journal of Chemical & Engineering Data* 48, no. 6 (2003): 1529-1539.
38. Shi, S., Wang, J., Liu, K., Jin, G. et al., "Vibro-Acoustic Modelling of the Box Structural–Acoustic Coupling System," *Results in Physics* 31 (2021): 104915.
39. Li, W., Chai, Y., Lei, M., and Liu, G., "Analysis of Coupled Structural-Acoustic Problems Based on the Smoothed Finite Element Method (S-Fem)," *Engineering Analysis with Boundary Elements* 42 (2014): 84-91.
40. Allemang, R.J., "A Correlation Coefficient for Modal Vector Analysis," in *Proceeding of the 1st IMAC*, Orlando, 1982, 110-116.

41. Oka, M., Enokizono, M., Mori, Y., and Yamazaki, K., "Magnetic Characterization of the Stator Core of a High-Speed Motor Made of an Ultrathin Electrical Steel Sheet Using the Magnetic Property Evaluation System," *AIP Advances* 8, no. 4 (2017): 1-8, doi:https://doi.org/10.1063/1.4993502.
42. Boubaker, N., Matt, D., Enrici, P., Nierlich, F. et al., "Measurements of Iron Loss in PMSM Stator Cores Based on Cofe and Sife Lamination Sheets and Stemmed from Different Manufacturing Processes," *IEEE Transactions on Magnetics* 55, no. 1 (2019): 1-9, doi:https://doi.org/10.1109/TMAG.2018.2877995.
43. Deng, W., Qian, Z., Chen, W., Qian, C. et al., "Orthotropic Material Parameters Identification Method of Stator Core and Windings in Electric Motors," *IEEE Transactions on Energy Conversion* 38, no. 4 (2023): 2464-2474, doi:https://doi.org/10.1109/TEC.2023.3276980.
44. Chai, F., Li, Y., Pei, Y., and Li, Z., "Accurate Modelling and Modal Analysis of Stator System in Permanent Magnet Synchronous Motor with Concentrated Winding for Vibration Prediction," *IET Electric Power Applications* 12, no. 8 (2018): 1225-1232, doi:https://doi.org/10.1049/iet-epa.2017.0813.
45. Torregrossa, D., Fahimi, B., Peyraut, F., and Miraoui, A., "Fast Computation of Electromagnetic Vibrations in Electrical Machines via Field Reconstruction Method and Knowledge of Mechanical Impulse Response," *IEEE Transactions on Industrial Electronics* 59, no. 2 (2012): 839-847, doi:https://doi.org/10.1109/TIE.2011.2143375.
46. Islam, M.S., Islam, R., and Sebastian, T., "Noise and Vibration Characteristics of Permanent-Magnet Synchronous Motors Using Electromagnetic and Structural Analyses," *IEEE Transactions on Industry Applications* 50, no. 5 (2014): 3214-3222, doi:https://doi.org/10.1109/TIA.2014.2305767.
47. Gieras, J., Wang, C., and Lai, J., *Noise of Polyphase Electric Motors*, 1st ed. (Boca Raton, FL: Taylor & Francis, 2006)
48. Simulia, "ABAQUS 2022 Analysis User Manual," Dassault Systemes Simulia Corp., 2022.
49. Sathyan, S., Aydin, U., and Belahcen, A., "Acoustic Noise Computation of Electrical Motors Using the Boundary Element Method," *Energies* 13, no. 1 (2020): 245, doi:10.3390/en13010245.